Supplementary Information for:

Defect Assisted Electronic Metal-Support Interaction: Tuning the Interplay Between Ru Nanoparticles and CuO Supports for pH Neutral Oxygen Evolution

Alexander J. Porkovich[a,*], Pawan Kumar[a], Zakaria Ziadi[a], David C. Lloyd[a], Lin Weng[a], Nan Jian[a,b], Toshio Sasaki[a], Mukhles Sowwan[a], Abheek Datta[a,*]

[a]Okinawa Institute of Science and Technology (OIST) Graduate University, 1919-1 Tancha, Onna-Son, Okinawa 904-0495, Japan
[b]Institute of Nanosurface Science and Engineering, Shenzhen University, Nanhai Ave. 3688, Shenzhen, Guangdong, China

Corresponding Authors
*E-mail: alexander.porkovich@oist.jp
*E-mail: datta.abheek@oist.jp

Section S1. Scanning Transmission Electron Microscopy (STEM) analysis of Ru nanoparticles (NPs) and identification of multiple Ru NP structures on CuO nanowires (NWs):

Section S2. Peak Force Kelvin probe microscopy (PF-KFPM) analysis of Ru NPs, CuO NWs and Ru NP decorated CuO NWs:

Section S3. X-ray photoelectron spectroscopy (XPS) analysis of Ru NP decorated CuO NWs:

Section S4. STEM analysis of Ru NPs on CuO NWs after annealing in dry air:

Section S5. Electrochemical characterisation of electrochemical surface area (ECSA) and electrochemical impedance spectroscopy (EIS):

Section S6. Post-Catalysis XPS and STEM:

Section S7. References

Section S1. Scanning Transmission Electron Microscopy (STEM) analysis of Ru nanoparticles (NPs) and identification of multiple Ru NP structures on CuO nanowires (NWs)

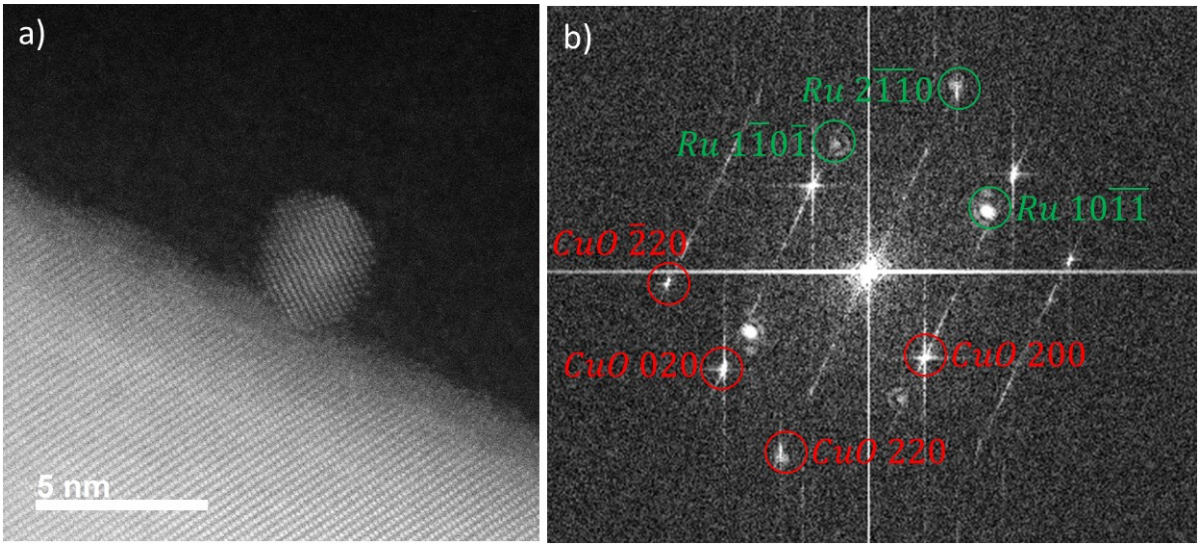

Figure S1. a) Full high-angle annular dark field STEM (HAADF-STEM) image of single crystal *hcp* Ru NP from Figure 1, while b) shows the indexed fast Fourier transform (FFT) of the Ru NP and the CuO NW. The Ru NP is visualised on its $[01\bar{1}1]$ zone axis, while the CuO NW is imaged along the $[001]$ direction.

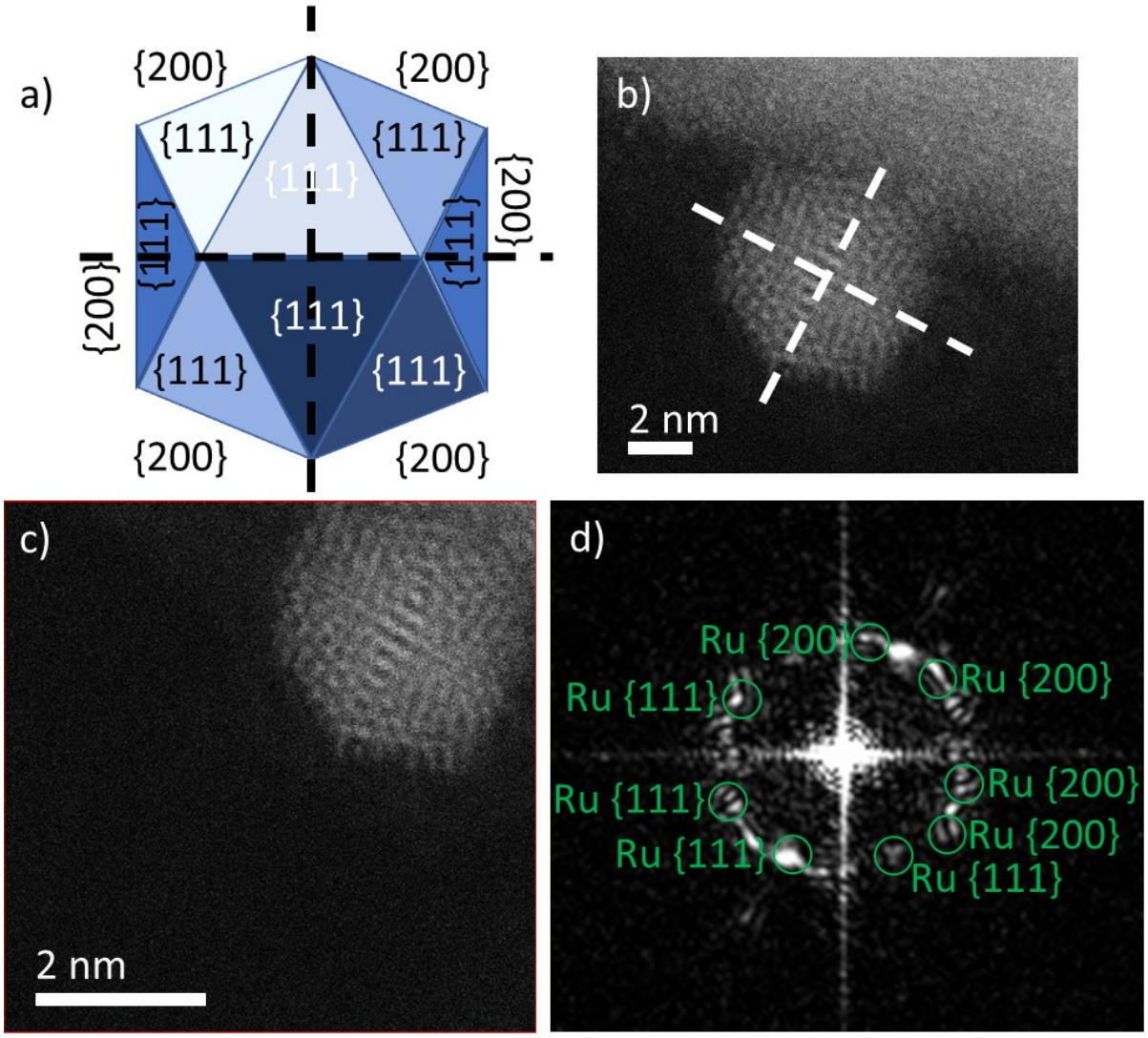

Figure S2. a) A schematic of an icosahedron viewed with 2-axes of symmetry, as denoted by the dashed black lines. This same 2-axis symmetry can be seen in the b) HAADF-STEM image (white dashed lines) which is the same as that viewed in Figure 1 of the main text. An area of this was selected in digital micrograph using the square tool, as seen in c), and the FFT of this area was taken and can be seen in d) showing interplanar spacing consistent with fcc Ru.

The size distribution and coverage of Ru NPs was determined by deposition of each of the samples on a bare carbon TEM grid. Multiple low magnification STEM images were used to gain as large a sample size as possible. The images were analysed using the software ImageJ. The images were converted to black and white images (*via* use of the gaussian blur and threshold tools) which could be analysed using the analyse particle function. In this case, the particles shape was assumed spherical, and the function gave a count of the nanoparticles in the image, and the area (*A*) of each particle. Using **Equation S2**, the diameter (*d*) of the particles can be calculated.

$$d = 2 \times \sqrt{\frac{A}{2\pi}} \qquad \textbf{(S2)}$$

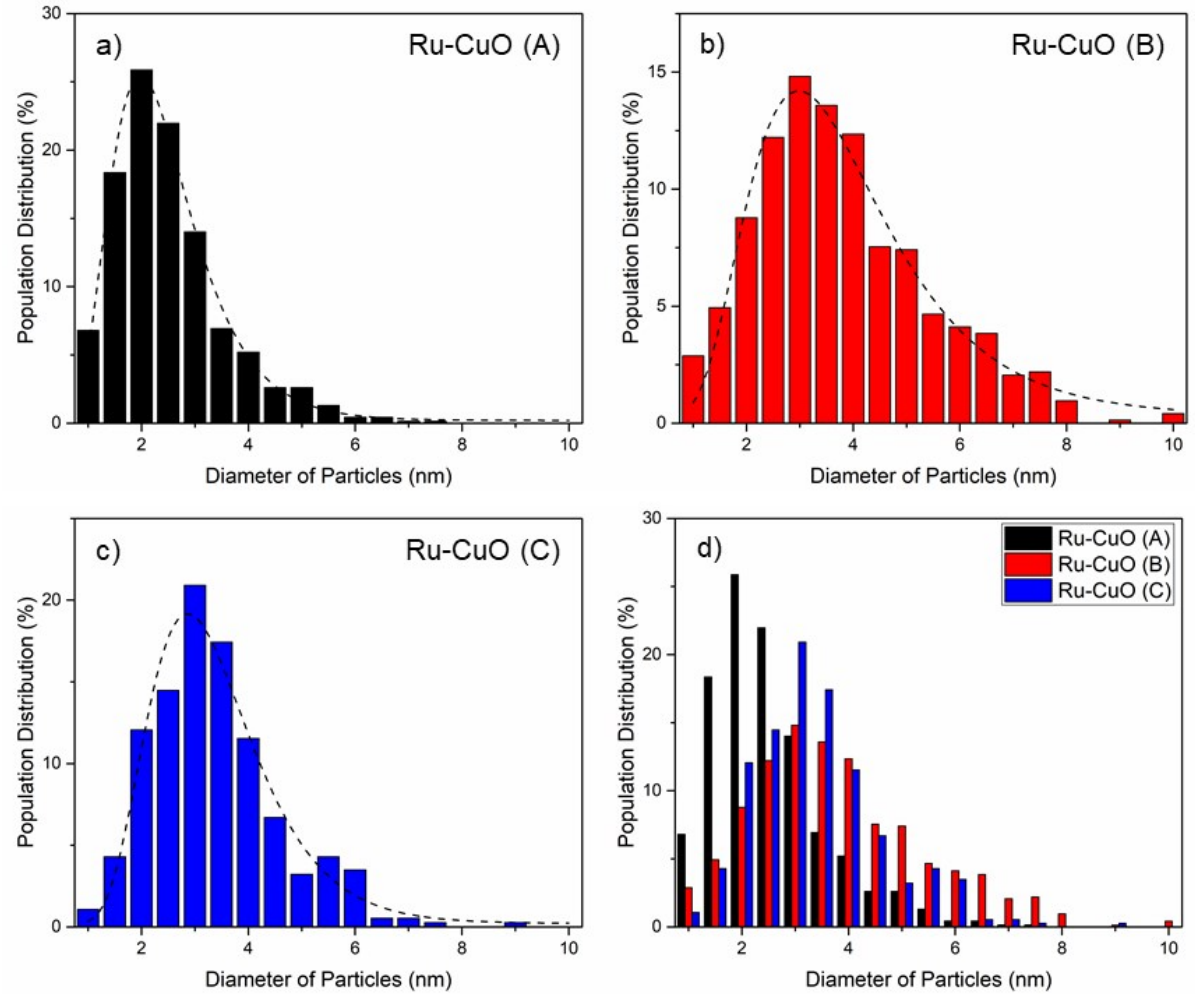

Figure S3. The size distribution of Ru NPs synthesised in samples a) Ru-CuO(A), b) Ru-CuO(B) and c) Ru-CuO(C). All samples can be viewed on d) the same axes for comparison.

The coverage of NPs can be calculated in multiple ways, the most straightforward is to calculate the coverage by taking the area of the image, counting how many nanoparticles are located there, and determining an answer in terms of np/cm^2. This technique was used in multiple images for each sample, before determining an average coverage from all images from a sample.

One issue with this way of describing coverage is that if NPs are different sizes, then it can be difficult to fully evaluate how much area is being taken up by the actual material of the NPs. An alternative way to calculate coverage is to determine the average size of the NPs (d_{av}). This is used to calculate an average area of each NP, which can then be multiplied by the number of NPs per unit of area ($\frac{n_{av}}{A_{cm^2}}$), to estimate a coverage fraction (C_F). This is also best averaged over multiple images for each sample to alleviate sampling errors.

$$\left(\frac{d_{av}}{2}\right)^2 \pi \times \frac{n_{av}}{A_{cm^2}} = C_F \qquad \textbf{(S3)}$$

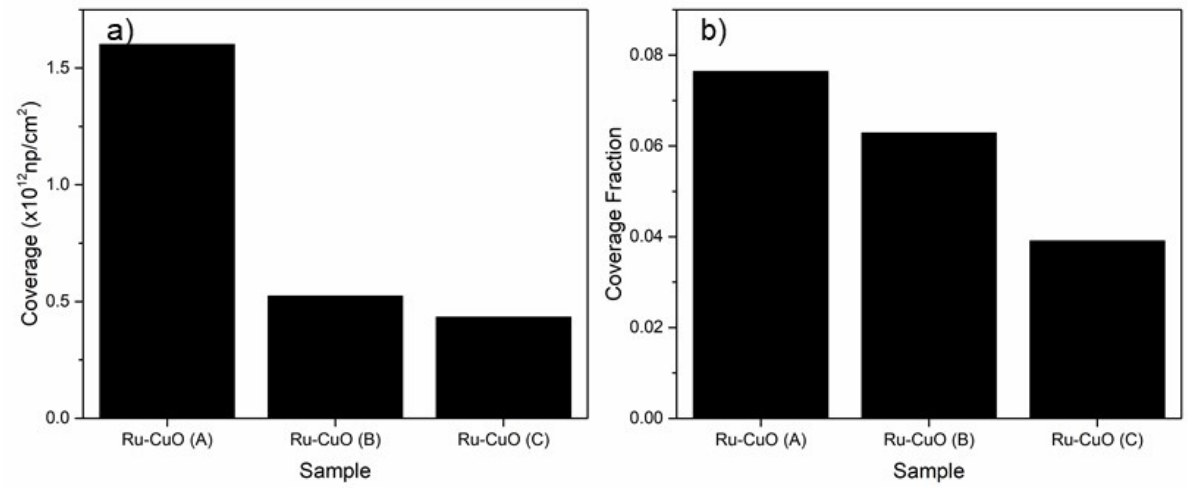

Figure S4. The coverage of Ru NPs deposited for each sample in terms of a) number of NPs per cm^2 and b) coverage fraction.

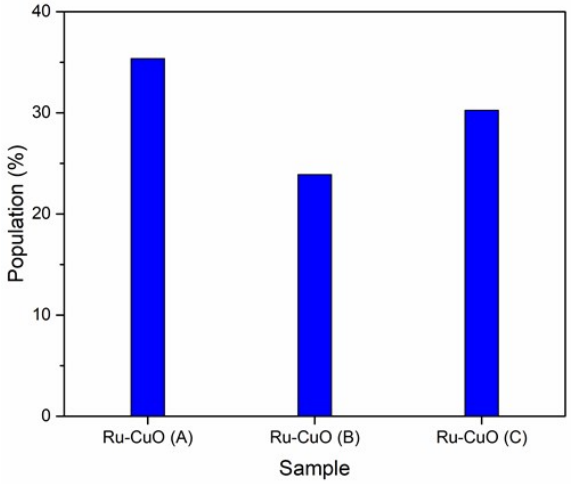

Figure S5. The amount of the Ru NPs in each sample which exist as aggregates rather than monodisperse NPs.

Section S2. PeakForce Kelvin probe microscopy (KFPM) analysis of Ru NPs, CuO NWs and Ru NP decorated CuO NWs

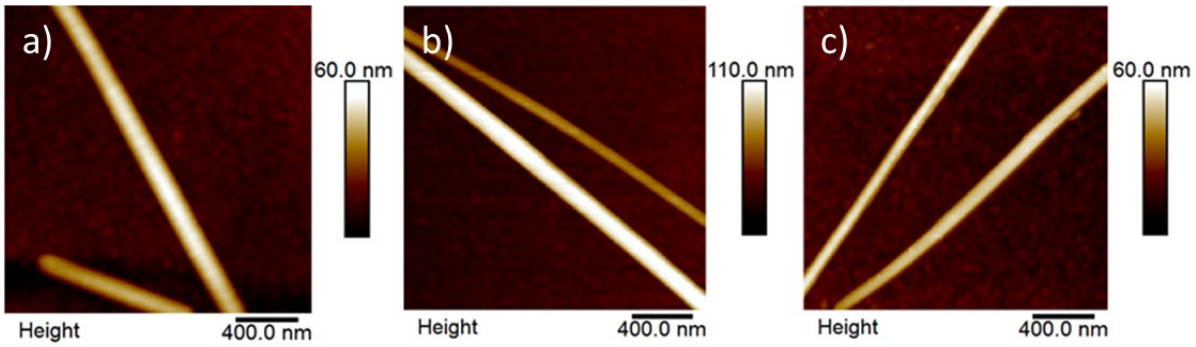

Figure S6. The topographic images corresponding to the potential images seen in figure 2 for a) Ru-CuO(A), b) Ru-CuO(B) and c) Ru-CuO(C).

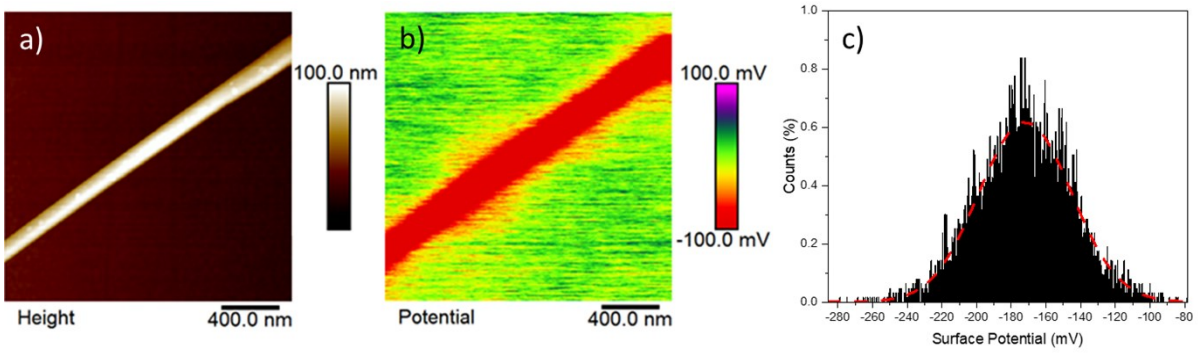

Figure S7. KPFM images showing a) topography and b) the surface potential of undecorated CuO NWs. The potential of the image can be expressed in terms of c) a histogram of the image seen in b) with a Gaussian distribution.

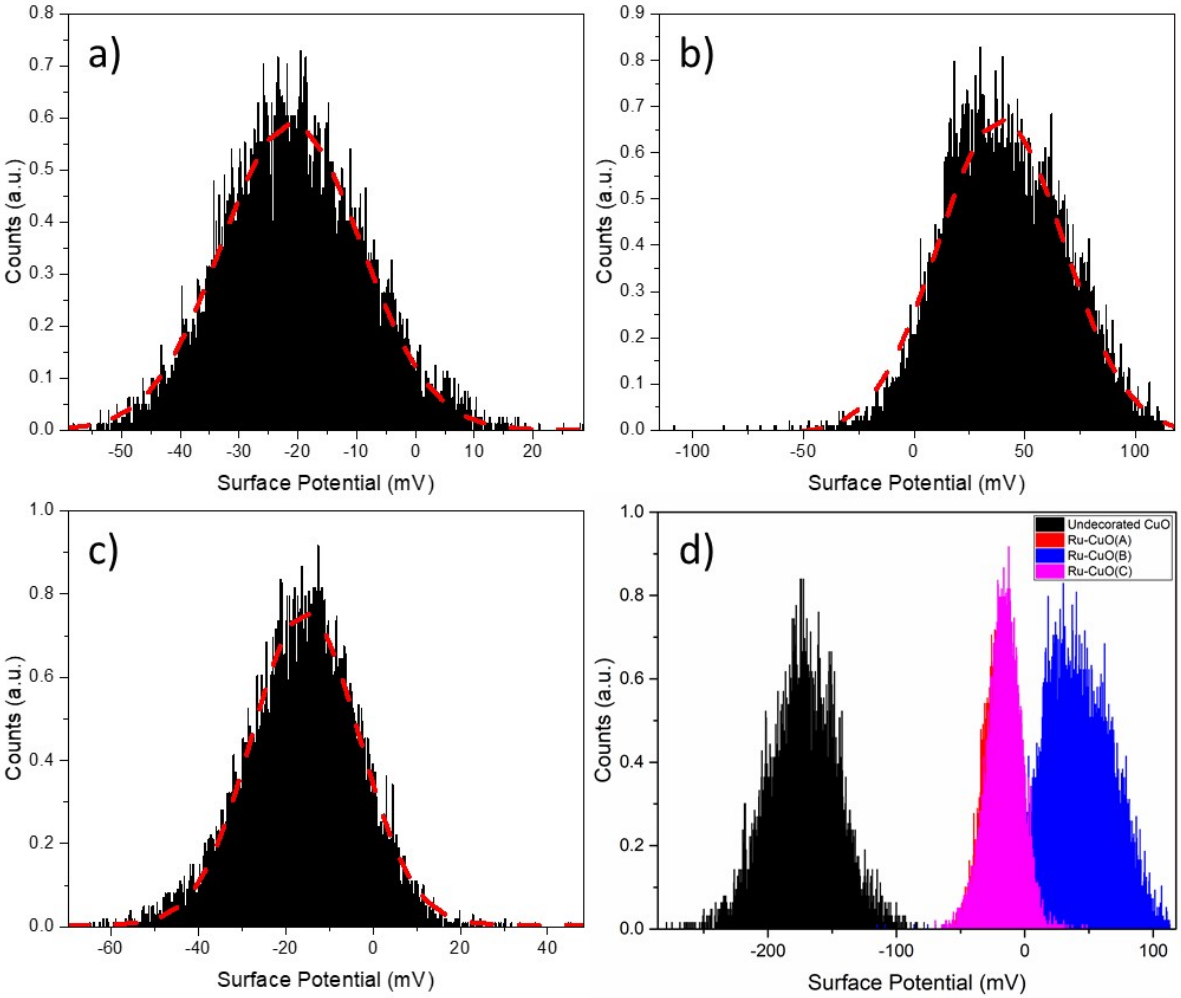

Figure S8. The distribution of surface potentials in the KFPM images for a) Ru-CuO(A), b) Ru-CuO(B) and c) Ru-CuO(C) which can be seen in **Figure 2**. These potentials have been plotted on the same axis in d), along with the distribution of surface potential in the undecorated CuO NW seen in **Figure S6**.

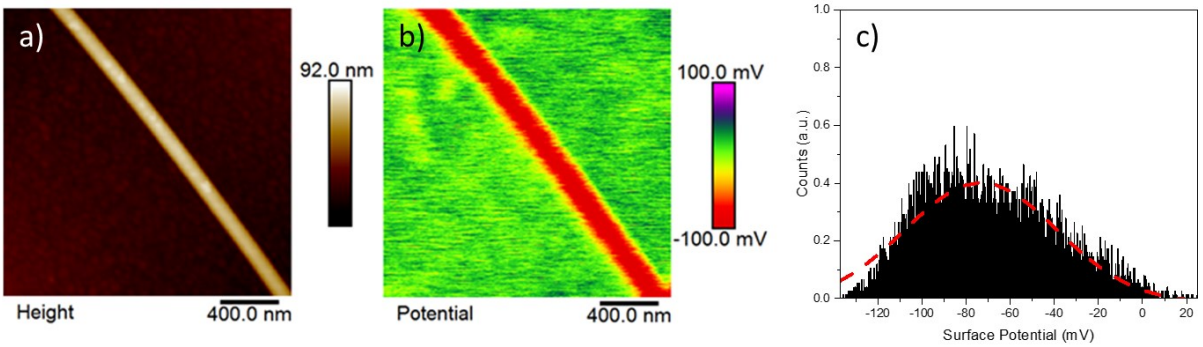

Figure S9. KPFM images showing a) topography and b) the surface potential of the increased deposition time (30 minutes) using the parameters from the Ru-CuO(C) sample. The potential of the image can be expressed in terms of c) a histogram with a Gaussian distribution.

Section S3. X-ray photoelectron spectroscopy (XPS) analysis of Ru NP decorated CuO NWs

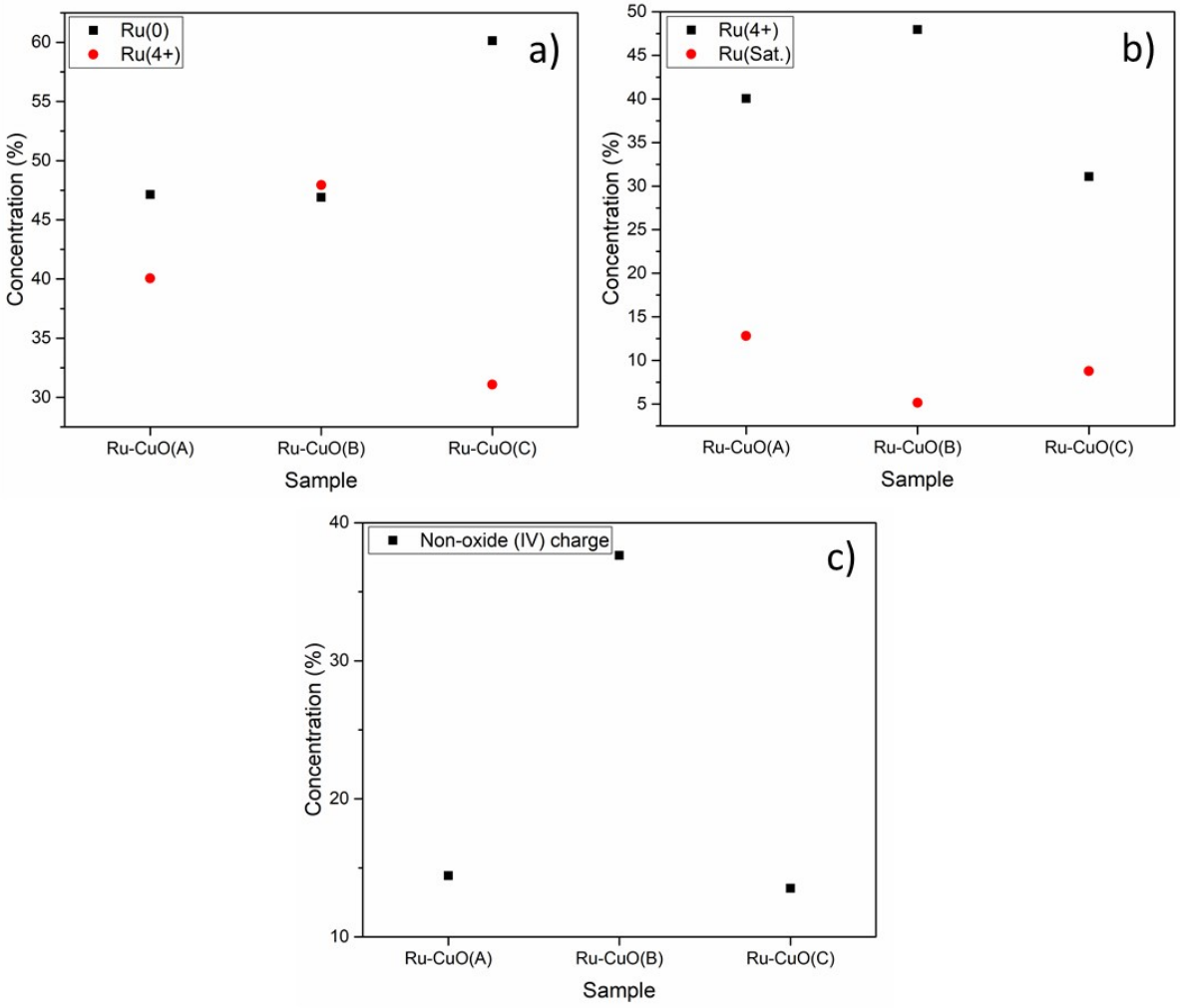

Figure S10. The relative ratio of the concentration of a) Ru^0 and Ru^{4+}, b) Ru4+ and RuO_2 sat, and the calculated concentration of Non-oxide Ru^{4+}.

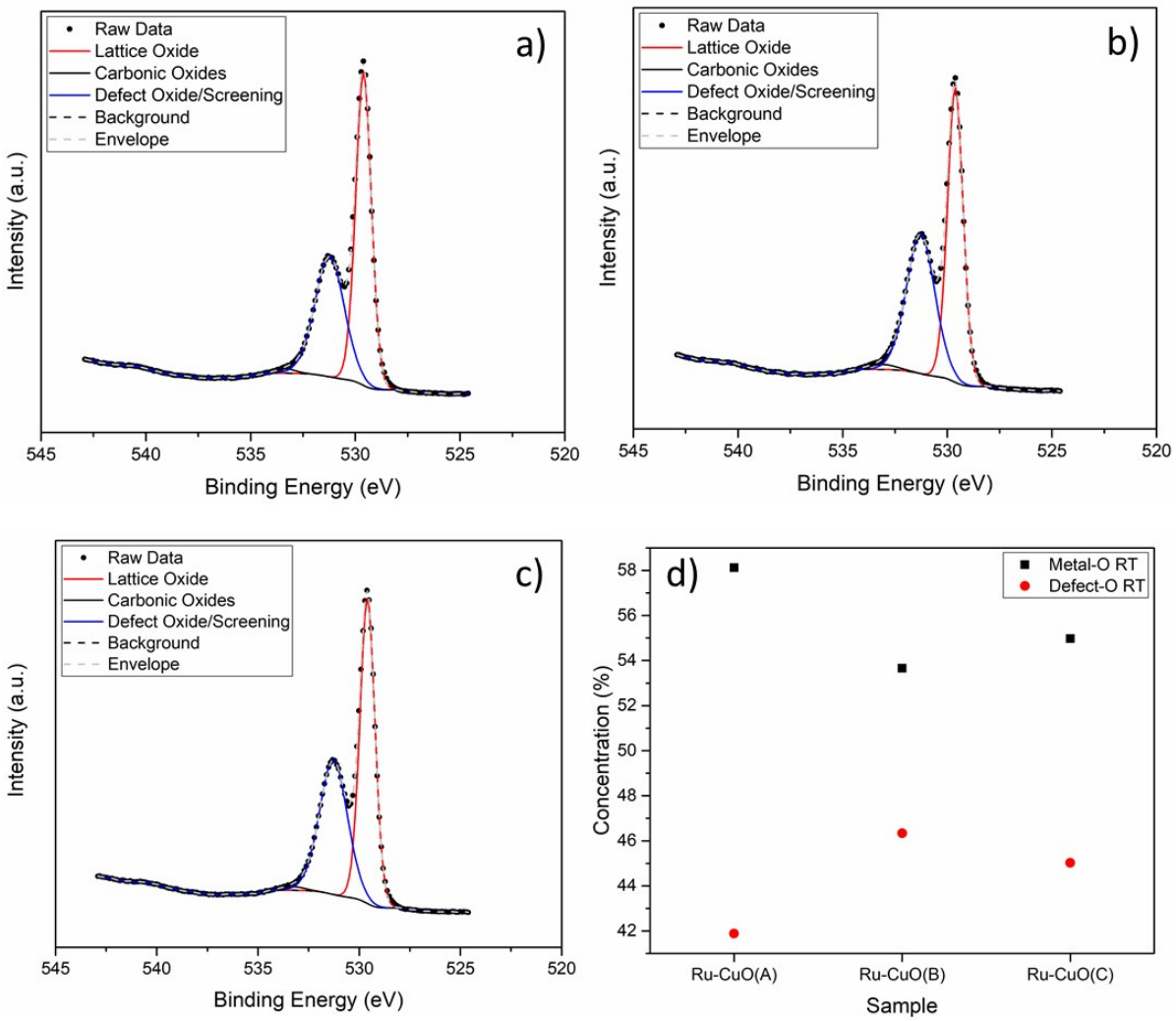

Figure S11. XPS spectra of the O 1s peak for a) Ru-CuO(A), b) Ru-CuO(B) and c) Ru-CuO(C). Raw data is represented by the black dot (●), while the dashed grey line represents the fitting envelope and the dashed black line represents the Shirley background. Red, blue and black lines represent deconvolutions of the lattice oxide in Cu, the defective oxide/vacancies in Cu, along with the metallic screening, and the carbonic oxide contributions respectively. The relative concentrations of lattice oxide (Metal-O) and defect oxide/screening (Defect-O) species is summarised in d).

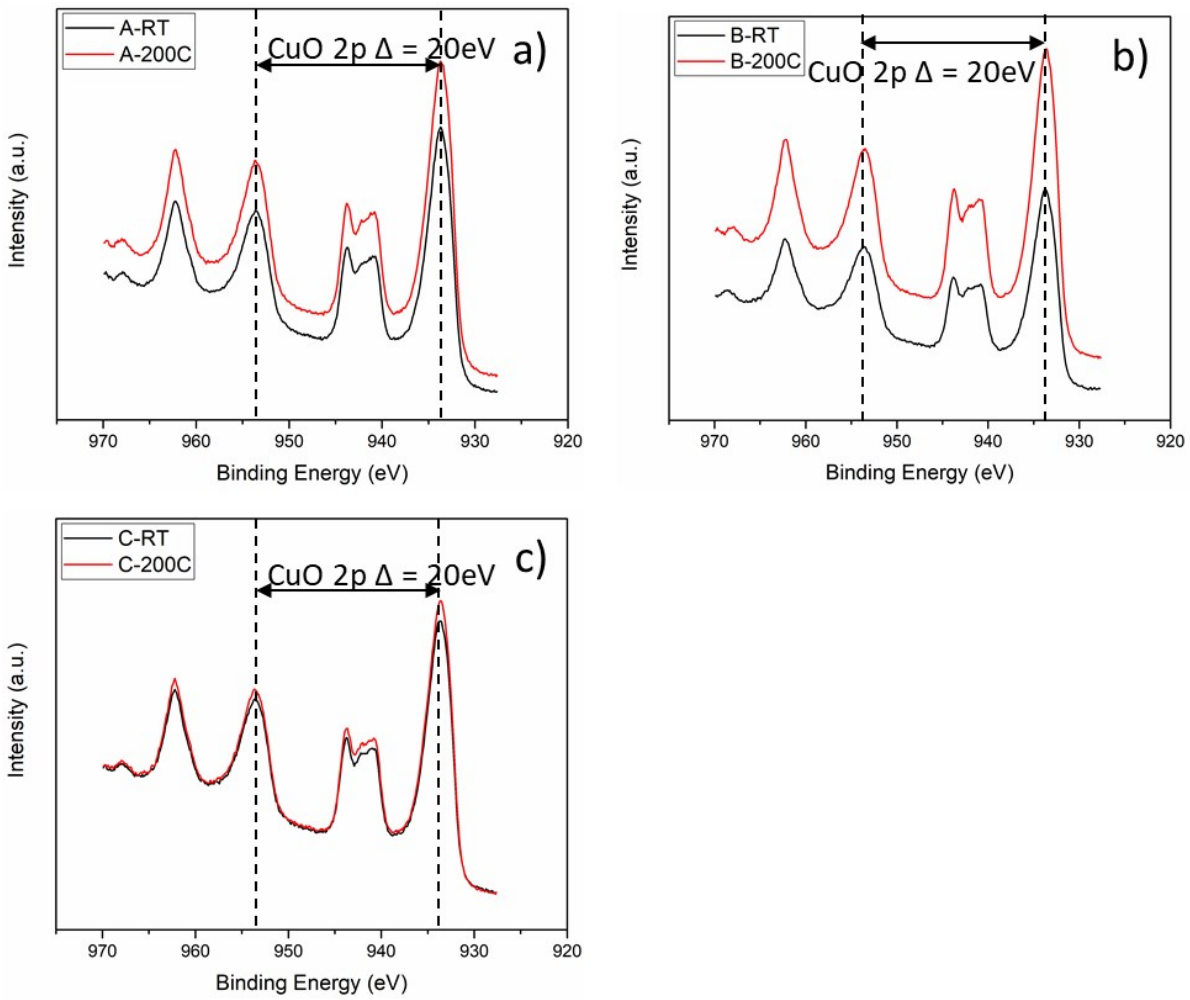

Figure S12. The Cu 2p XPS spectra of as deposited (RT) and annealed for 3hrs at 200°C (200C) for samples a) Ru-CuO(A), b) Ru-CuO(B), and c) Ru-CuO(C). Spin-orbit splitting of 20eV (marked with dashed black lines) is typical for CuO.

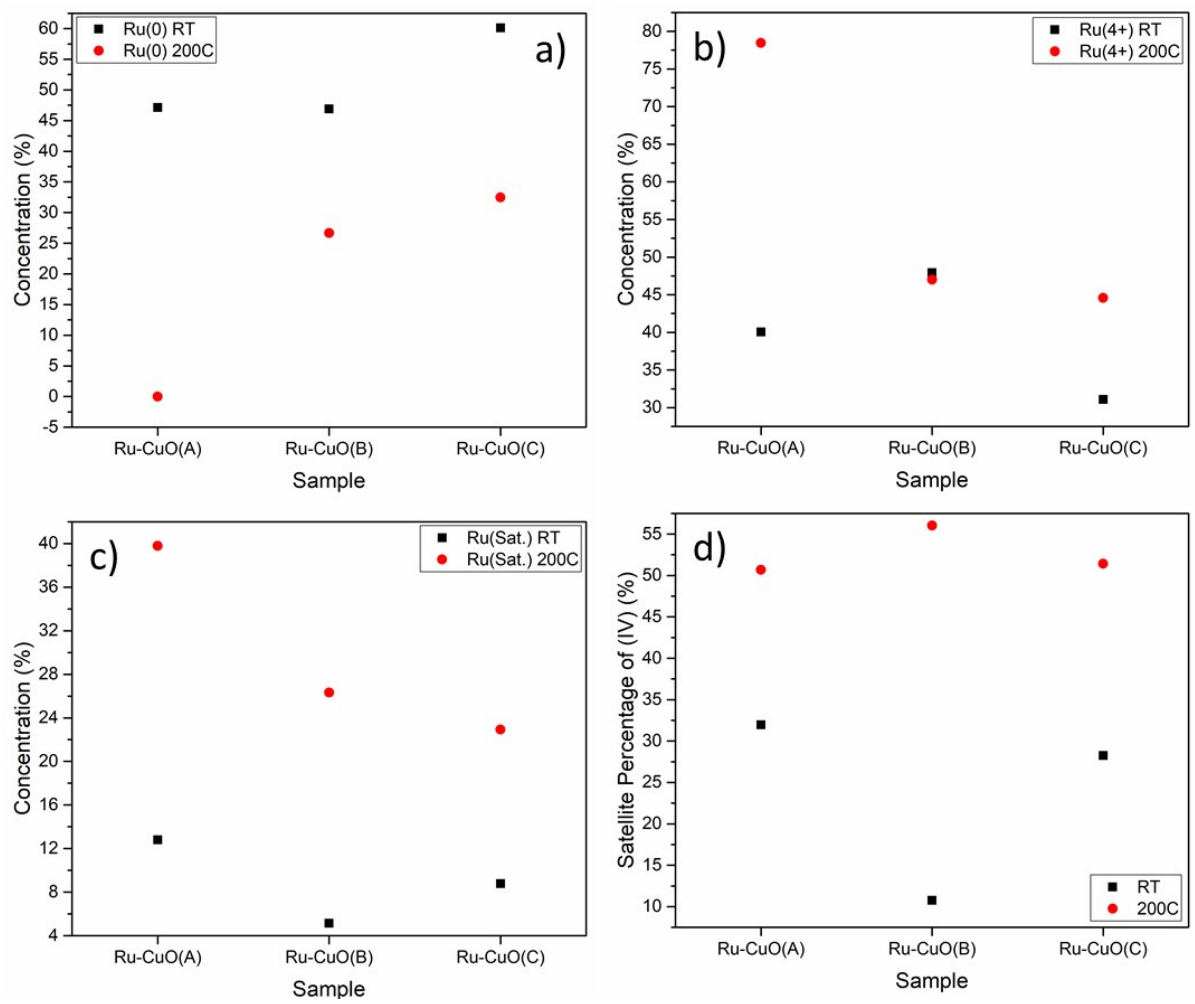

Figure S13. The relative ratio of the concentration of a) Ru^0, b) Ru^{4+} and c) RuO_2 sat. as deposited (RT) and after annealing for 3hrs at 200°C. The percentage of Ru^{4+} which exists as RuO_2 is seen in d), for the same samples.

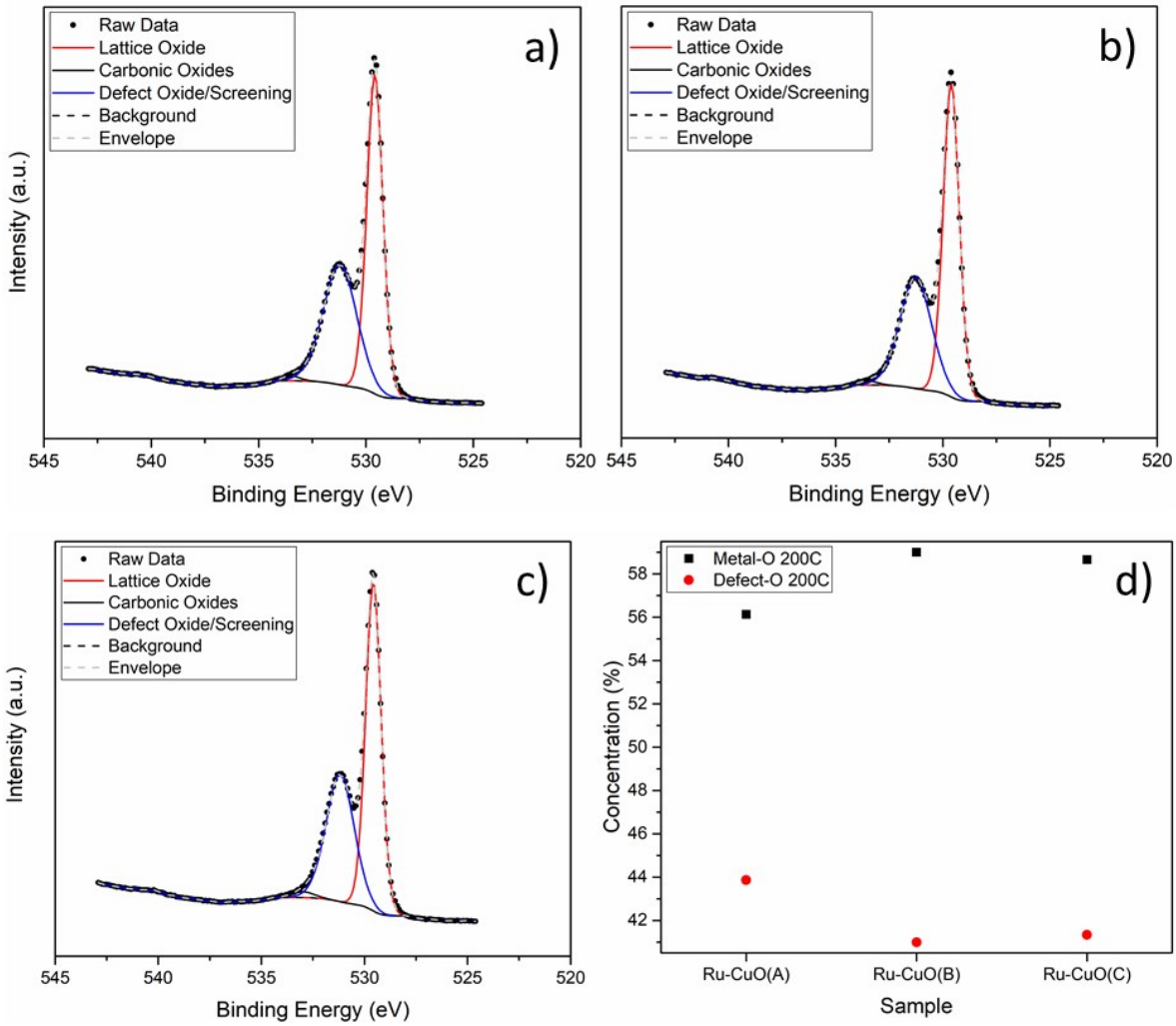

Figure S14. XPS spectra of the O 1s peak for a) Ru-CuO(A), b) Ru-CuO(B) and c) Ru-CuO(C) after annealing at 200°C for 3 hrs. Raw data is represented by the black dot (●), while the dashed grey line represents the fitting envelope and the dashed black line represents the Shirley background. Red, blue and black lines represent deconvolutions of the lattice oxide in Cu, the defective oxide/vacancies in Cu, along with the metallic screening, and the carbonic oxide contributions respectively. The relative concentrations of lattice oxide (Metal-O) and defect oxide/screening (Defect-O) species is summarised in d).

Section S4. STEM analysis of Ru NPs on CuO nanowires NWs after annealing in dry air

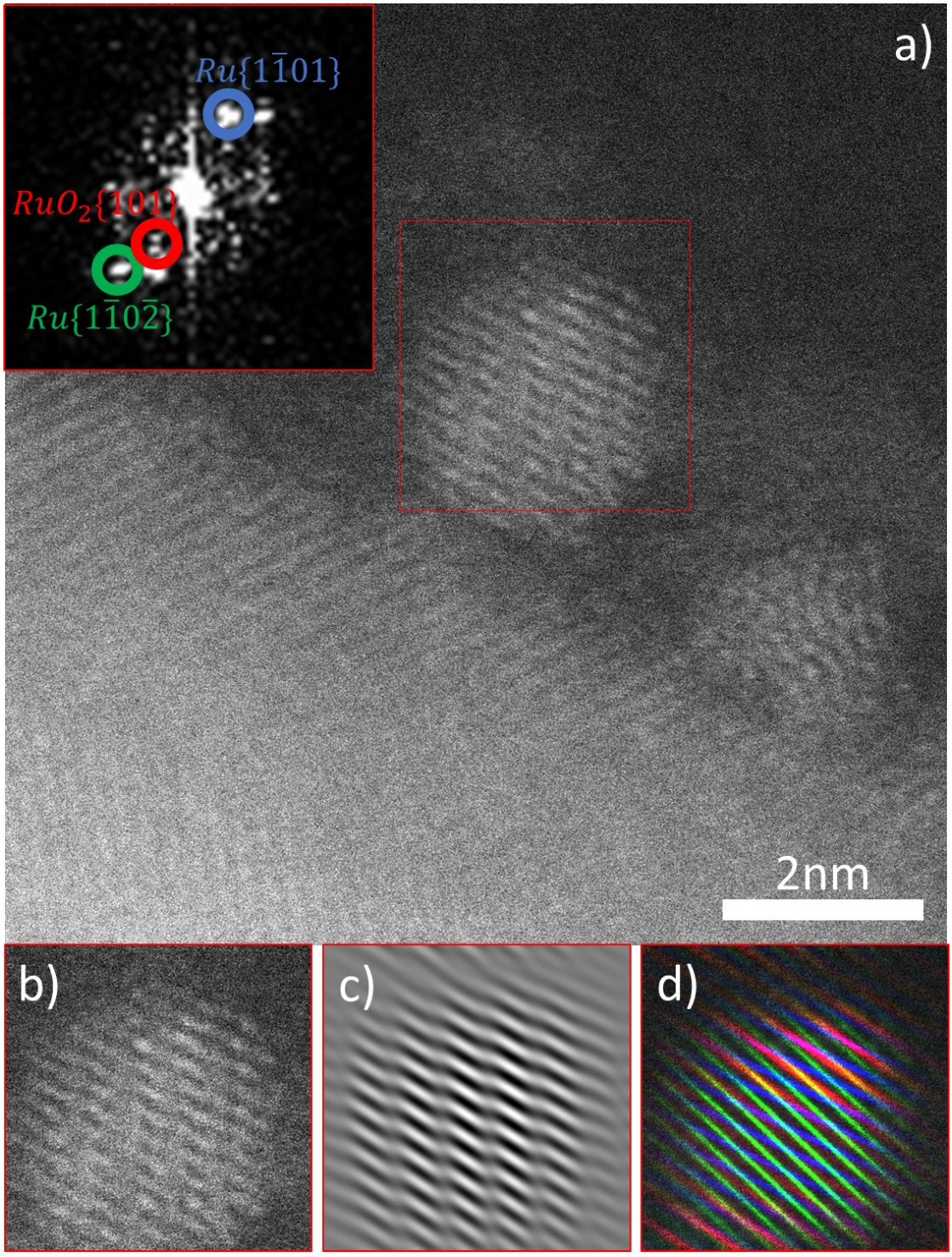

Figure S15. a) A STEM-HAADF image of *hcp* Ru NPs on a CuO NW annealed in dry air for 100min at 200°C. The inset FFT is from the area in the image marked by the red square. The Inverse of this FFT can be seen in b) showing defects. These defects are highlighted by applying Bragg filtering to the spatial frequencies for Ru $\{1\bar{1}01\}$ and Ru $\{1\bar{1}0\bar{2}\}$, resulting in the image seen in c). Finally, d) shows a false colour image imposed on b), highlighting the planes belonging to Ru $\{1\bar{1}01\}$, Ru $\{1\bar{1}0\bar{2}\}$ and RuO_2 {101} in blue, green and red respectively.

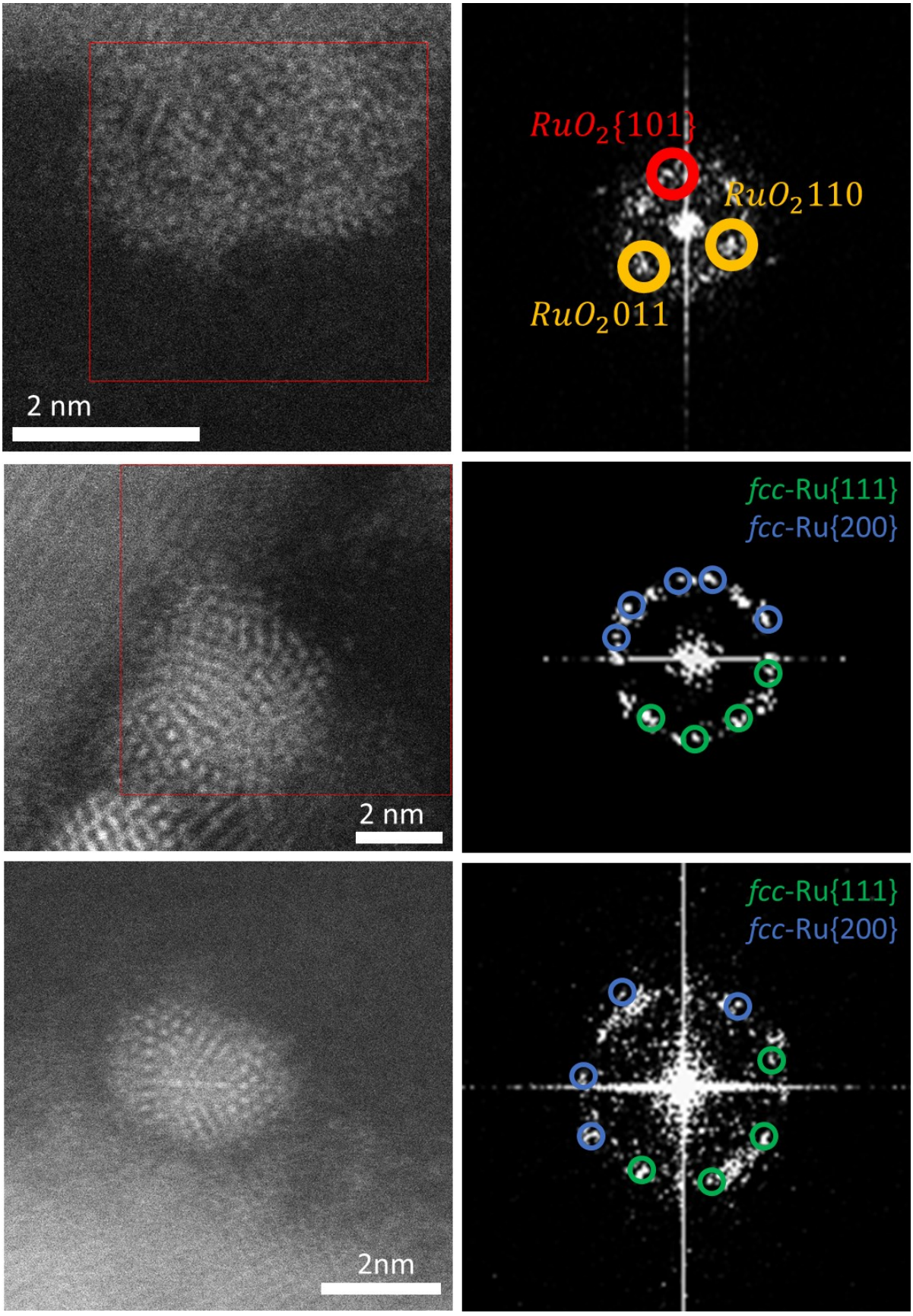

Figure S16. The images seen in figure 3 with indexed FFTs. All FFTs are the same as their inset counterparts in the main text, just enlarged.

Section S5. Electrochemical characterisation of electrochemical surface area (ECSA) and electrochemical impedance spectroscopy (EIS)

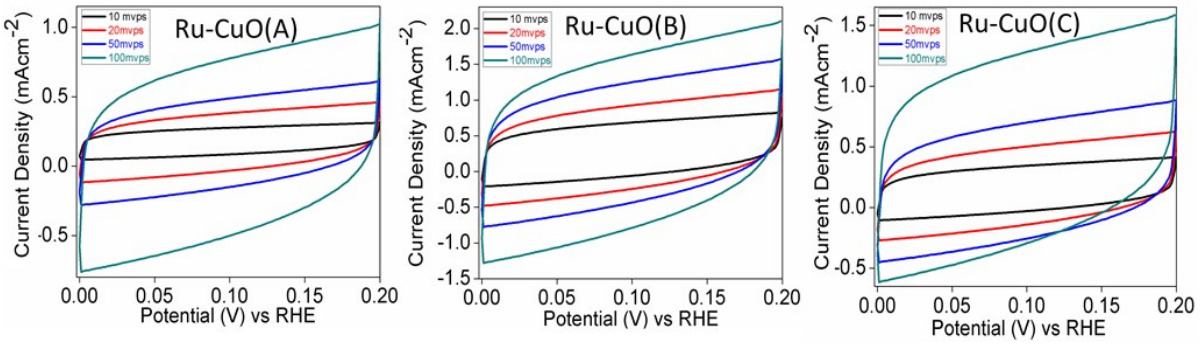

Figure S17. Cyclic voltammograms for Ru-CuO catalysts at non-faradic regions.

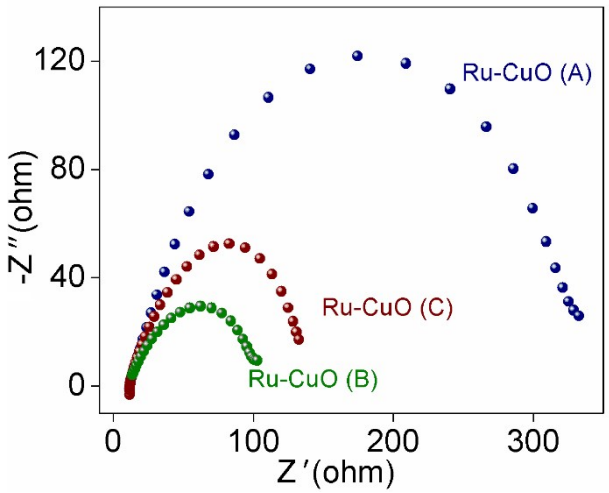

Figure S18. EIS plots for OER activities of Ru-CuO catalysts at neutral pH.

Section S6. Post-Catalysis XPS and STEM

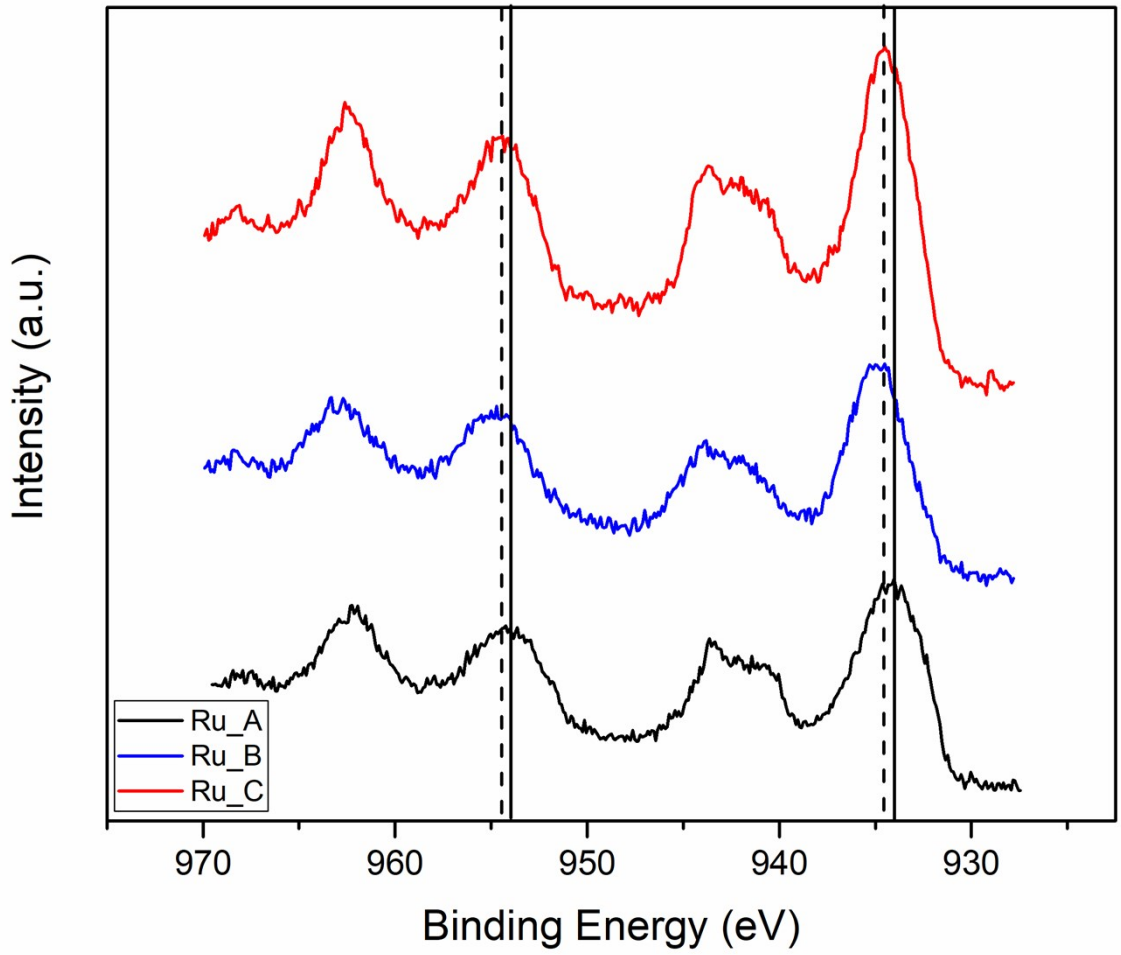

Figure S19. Cu *2p* XPS spectra for Ru-CuO(A) (black), Ru-CuO(B) (blue) and Ru-CuO(C) (red) samples following catalysis. The solid black line indicates the position of the CuO doublet, while the dotted black lines represent the $Cu(OH)_2$ doublet positions.[4]

The Cu *2p* XPS spectra post catalysis for all three samples can be seen in **Figure S19**. Each sample resembles an amalgamation of the shape of a CuO and $Cu(OH)_2$ XPS spectra (including peaks positions and the shape of the satellite shake up peak at ~940 eV).[4] There are obvious differences between each sample, including peak position (as seen by the solid line for the CuO doublet, and the dotted line for $Cu(OH)_2$) and shape of the satellite. For Ru-CuO(A), the Cu $2p_{3/2}$ peak is at 933.7 eV (CuO), but slightly broadened, indicating that while $Cu(OH)_2$ has been formed,[4] the Cu in this sample is more oxide than hydroxide. In contrast, Ru-CuO(B) (with a higher proportion of multiple twin particles) shows a Cu $2p_{3/2}$ XPS spectra with a positive shift towards 934.67 eV ($Cu(OH)_2$).[4] There has also been a change to the 940 eV satellite. In this case, while there is some CuO still remaining (as seen from the broad peak), it is apparent, that there has been a much greater formation of hydroxide species on the Cu. Finally, the Ru-CuO(C) Cu $2p_{3/2}$ spectra is in between the two other samples in terms of peak position, and the shape of the satellite. This would mean that the sample with multiple twins and more agglomerates has resulted in slightly more hydroxylated Cu than the single crystal dominated sample (Ru-CuO(A)), but less so than the sample with more multiple twins (Ru-CuO(B)).

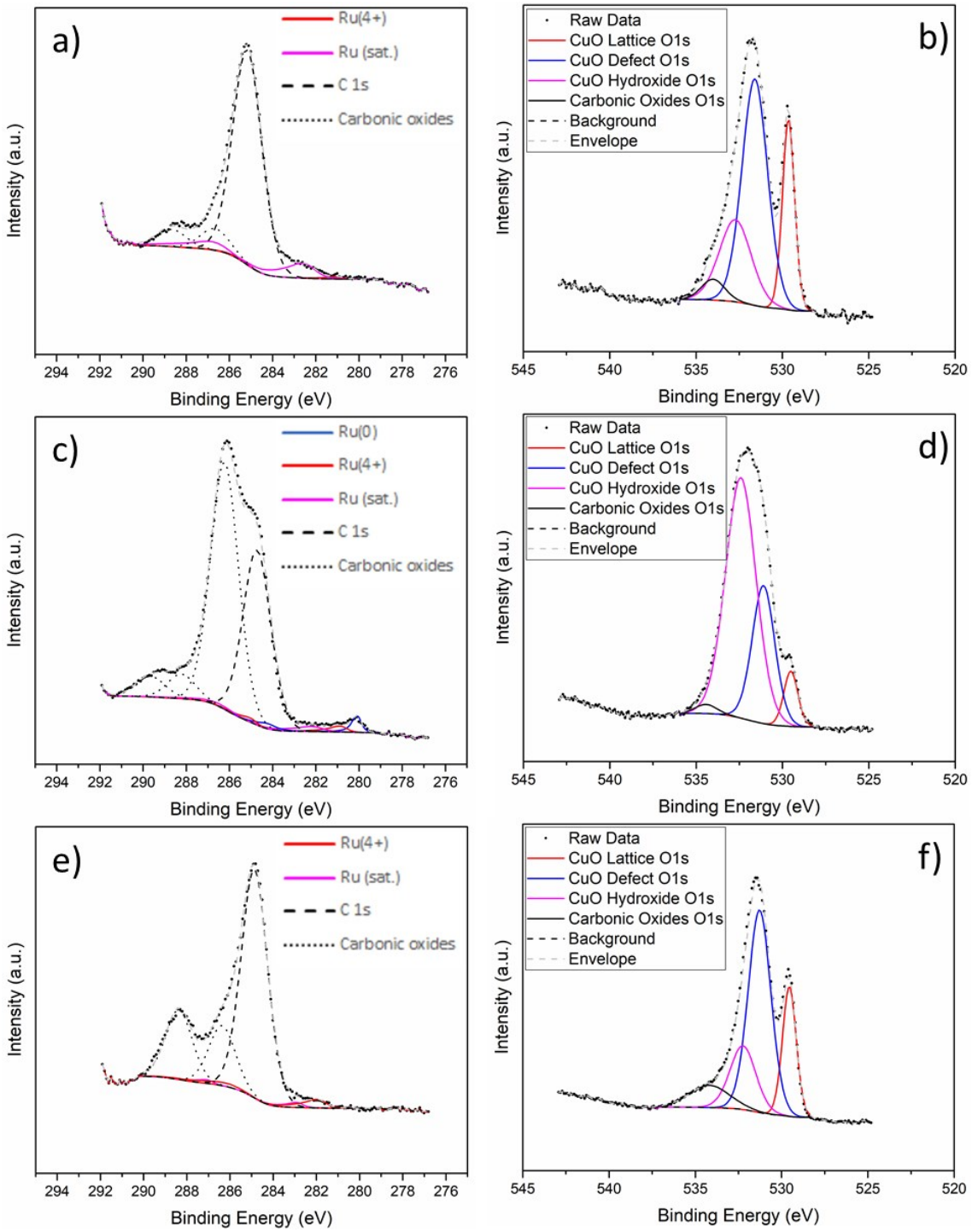

Figure S20. XPS spectra of the samples post catalysis for the Ru *3d* (a), c) and e)) and O *1s* (b), d) and f)) regions. Ru-CuO(A) spectra is seen in a) and b), Ru-CuO(B) in c) and d), and Ru-CuO(C) in e) and f). Shirley background is indicated by a dashed black line, while the dashed grey line indicates the fitting envelope or sum. All peaks are indicated in the legend of each figure.

The Ru *3d*, C *1s* and O *1s* areas of the XPS spectra of the post catalysis samples can be seen in **Figure S20**. In **Figure S20 a and b**, the spectra for Ru-CuO(A), Ru-CuO(B) can be seen in **Figure S20 c and d**, and Ru-CuO(C) is shown in **Figure S20 e and f**. The Ru species in Ru-CuO(A) are primarily seen around 281 eV (8%) and 282.4 eV (92%), indicating the Ru is fully oxidized.[2] The C species primarily exist as adventitious carbon species, and two oxide species (assigned to C-OH, 286.4 eV, and C=O at 288.4 eV)[3]

of much lower concentration. Finally, the lattice oxide species have decreased significantly (from the as deposited samples), while defect species have increased, along with hydroxide (from the Cu)[4] and a small concentration of carbonic oxides.[3]

The Ru-CuO(B) sample (higher concentration of multiple twins) on the other hand feature some stark differences. Most clearly is the higher concentration of Ru(0) or metallic species (~40% of total Ru species) at 280eV.[2, 3] This strongly correlates to the oxidation experiments highlighting that samples containing more multiple twins stay metallic during catalysis. In addition to this observation however, there are also substantial differences between the carbonic and oxide species of these samples. Firstly, the C-OH peak has increased dramatically in concentration (along with another carbonic oxide peak related to O-C=O),[3] as has the hydroxide peak in the O *1s* spectra. This is strongly indicates that far more OH species are formed during catalysis with the multiple twin samples than the single crystal samples (Ru-CuO(A)), approximately a 5-fold increase in C-OH and 3-fold increase in hydroxides related to Cu.

Finally, sample Ru-CuO(C) (with more agglomerates) has similar concentration of carbonic and oxide species as Ru-CuO(A) (though there is more oxidised carbon species in Ru-CuO(C)). However, the Ru species more prevalent in this sample is Ru(4+) (as opposed to the Ru satellite which is most prevalent in Ru-CuO(A)), indicating the sample is less oxidized than the single crystal sample. The difference between the oxidation observed here, and the oxidation observed in the gaseous environments is likely due to the increased deposition time (20 min to 30 min) required to standardize the particle distributions for the electrocatalytic experiments. This is supported by the changes observed in the KPFM measurements of the Ru-CuO(C) samples deposited for 20 minutes (**Figure 2**) and 30 minutes (**Figure S9**).

All concentration data for each sample is summarized in **Figure S21**.

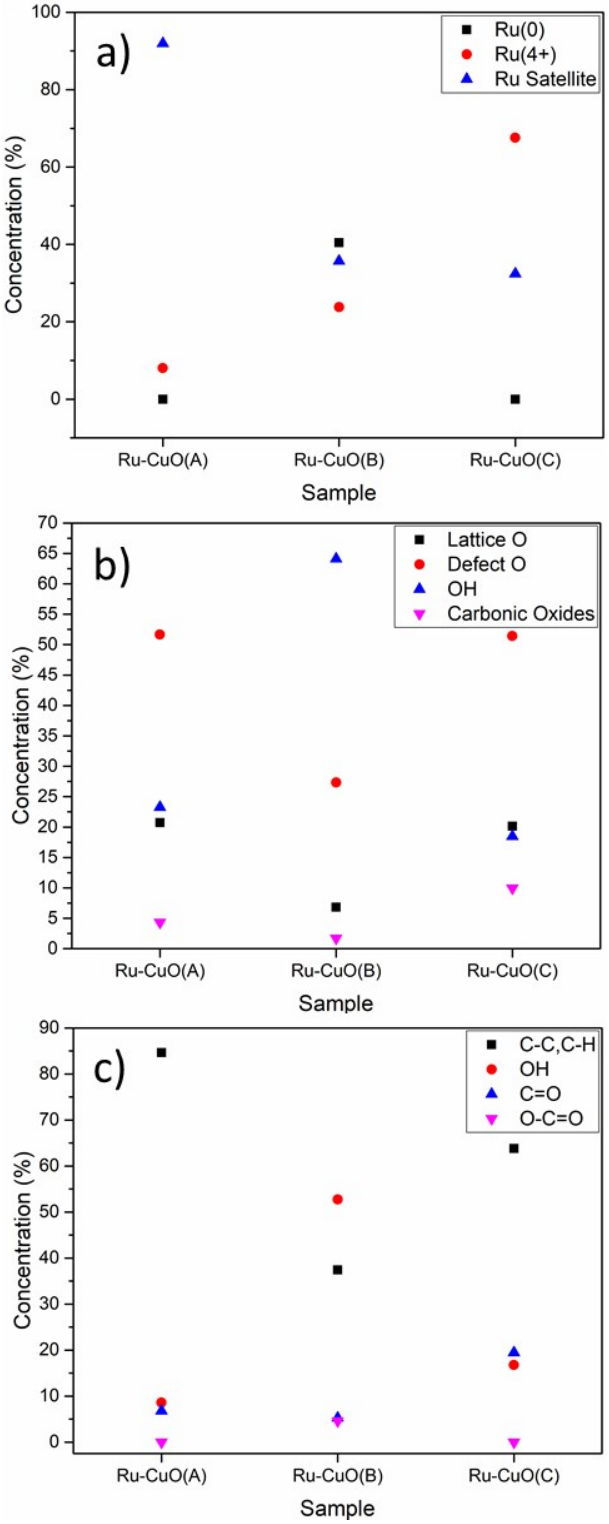

Figure S21. Relative concentrations of chemical order determined by XPS of samples after catalysis. Shown here is the relative concentrations of a) Ru species, b) oxygen species and c) carbon species.

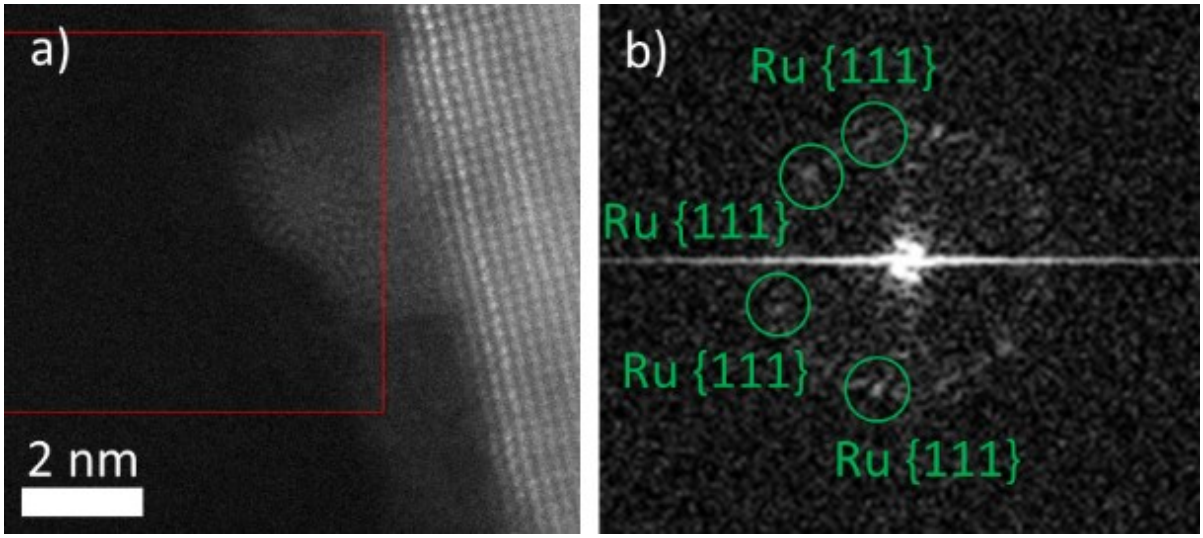

Figure S22. A STEM-HAADF image of a metallic icosahedral Ru NP can be seen in a) likely near the 3-fold axis. This image was taken on a sample that had been through a stability test. The corresponding FFT (taken from the area in the red square) in b) shows spots which can be indexed to metallic fcc Ru {111}.

Section S7. References

1. E. A. Paoli, F. Masini, R. Frydendal, D. Deiana, C. Schlaup, M. Malizia, T. W. Hansen, S. Horch, I. E. L. Stephens and I. Chorkendorff, *Chem. Sci.*, 2015, **6**, 190-196.
2. D. J. Morgan, *Surf. Interface Anal.*, 2015, **47**, 1072–1079.
3. J. F. Moulder, W. F. Stickle, P. E. Sobol and K. D. Bomben, *Handbook of X-Ray Photoelectron Epectroscopy: A Reference Book of Standard Spectra for Identification and Interpretation of XPS Data*, ULVAC-PHI, Chigasaki, Japan, 1995.
4. M. C. Biesinger, *Surf. Interface Anal.*, 2017, **49**, 1325–1334.
5. A. Porkovich, Z. Ziadi, P. Kumar, J. Kioseoglou, N. Jian, L. Weng, S. Steinhauer, J. Vernieres, P. Grammatikopoulos and M. Sowwan, *ACS Nano*, 2019, **13**, 12425−12437.
6. G. Greczynski and L. Hultman, *ChemPhysChem*, 2017, **18**, 1507-1512.